Available online at www.sciencedirect.com
ScienceDirect
Trans. Nonferrous Met. Soc. China 34(2024) 3846−3861
Transactions of Nonferrous Metals Society of China
www.tnmsc.cn

Effects of solute supersaturation and re-precipitation on microstructure and mechanical properties of selective laser melted Al−Mn−Mg−Sc−Zr alloys

Ying DENG[1], Yi LAI[1], Jia-shun CHEN[1], Yuan-hao XU[1], Jun-chang CAO[1], Rui-yin HUANG[2], Jia-qi DUAN[3]

1. School of Materials Science and Engineering, Central South University, Changsha 410083, China;
2. China Aluminum Materials Application Research Institute Co., Ltd., Beijing 102209, China;
3. Warwick Manufacturing Group, The University of Warwick, Coventry, CV4 7AL, UK

Received 30 June 2024; accepted 18 November 2024

Abstract: A new Al−4.87Mn−1.42Mg−0.63Sc−0.20Zr (wt.%) alloy was fabricated by selective laser melting (SLM) and its microstructure and mechanical properties before and after aging were investigated. The results show that at a laser power input of 300 W, increasing laser scanning speeds from 700 to 1500 mm/s improves the mechanical properties. In the meantime, the lattice distortion values increase from 0.15% to 0.31%, showing an increasing solute supersaturation. At a laser scanning speed of 1500 mm/s, the yield strength, ultimate tensile strength and elongation of the as-SLM alloys are 356 MPa, 412 MPa and 17.7%, respectively. After aging at 350 °C for 8 h, these values increase to 527 MPa, 554 MPa and 10.4%, respectively. The contributions to the yield strength increments from the secondary Al_6(Fe,Mn) needle-like phase and re-precipitated $L1_2$ structured Al_6(Sc,Zr,Ti) nano-particles during aging are 74 and 79 MPa, respectively. As the aging temperature increases to 450 °C, the dominant precipitation strengthening is attributed to the secondary Al_6(Sc,Zr,Ti) nano-particles.

Key words: Al−Mn−Mg alloy; selective laser melting; re-precipitation; solute atom; microstructure; mechanical properties

1 Introduction

Aluminum alloys are highly promising materials due to their exceptional specific strength, making them ideal for use in aerospace, marine transportation, and automotive industries [1−3]. In engineering applications, internal structure with high geometric complexity and high precision poses significant challenges to traditional manufacturing methods for aluminum alloys. The powder-bed fusion technique, i.e., selective laser melting (SLM), enables the fabrication of complex 3D-structures with unprecedented design freedom. SLM also shows potential for reducing the cost and saving the design-to-manufacture time [4−6].

In recent years, the production of high-strength aluminum alloys by SLM method has attracted increasing attention. The fast heating and rapid solidification during SLM lead to the formation of supersaturated solid solution with excessive alloying elements such as Mg, Mn and Zn, which can be exploited to enhance the performances of aluminum alloys [7−10]. Manufacturing parameters of SLM significantly affect on the solute super-saturation and strength of the SLM-fabricated aluminum alloys. LAI et al [11] highlighted the importance of optimizing SLM processing parameters to achieve high-strength of the SLM-fabricated Al−Mn−Mg alloys. JIA et al [12] indicated that the aluminum alloy components produced via SLM could achieve high strength when

Corresponding author: Rui-yin HUANG, Tel: +86-13600850963, E-mail: ruiyin_huang@chinalco.com.cn
DOI: 10.1016/S1003-6326(24)66643-4

the laser energy density exceeds 135 J/mm^3. DU et al [13] found that using optimized SLM processing parameters, a tensile strength of more than 426 MPa was achieved in Al−Mn−Sc−Zr alloys, due to the high cooling rate during the SLM that resulted in supersaturation. Nonetheless, the relationship between SLM processing parameters and solute supersaturation, and their effect on the strength of SLM-fabricated aluminum alloys are still unclear.

Scalmalloy is the first commercially available Sc-modified alloy specifically developed for additive manufacturing (AM). Owing to the Sc addition, a yield strength of 290 MPa and an elongation exceeding 15% have been reported in the as-SLM condition [14]. Further studies showed that superior mechanical properties of Scalmalloy were due to the formation of fine equiaxed grains and the precipitation of Al_3(Sc,Zr) phase during SLM [15]. LI et al [16] found that Al_3(Sc,Zr) nanoparticles precipitated during aging treatment of a Sc and Zr modified Al−8.0Mg−1.3Si−0.5Mn−0.5Sc−0.3Zr SLM alloy could enhance the tensile strength by 53 MPa. Recently, a Sc-modified 3xxx alloy system, i.e., Al−Mn−Mg−Sc−Zr, has been designed for the SLM, which showed even better mechanical properties than the Scalmalloy, with a yield strength of 430 MPa and an elongation of 19%. It was further found that such excellent mechanical properties were mainly attributed to the solution strengthening of Mn and Mg solute atoms and precipitation strengthening from Al_3(Sc,Zr) [17−22]. The precipitation strengthening can be optimized in the subsequent heat treatment process to re-precipitate secondary phases. WANG et al [17] showed that after aging treatment, a large number of spherical coherent $L1_2$-Al_3Zr particles with a mean radius of approximately 1.15 nm were re-precipitated and the aged alloys showed a higher strength than the as-SLM Al−Cu−Mg−Zr alloys. ZHANG et al [18] found that secondary phases Al_3(Er,Zr) uniformly precipitated in the matrix with a size of 5−20 nm after post-heat treatments of the laser powder bed fused Al−Zn−Mg−Cu−Si−Zr−Er alloys and significantly increased the strength. However, the study on the re-precipitation after post-heat treatments for the new Sc-modified 3xxx alloy system and their effects on mechanical properties is still lacking.

In this work, Sc and Zr modified Al−Mn−Mg alloy powders were selective laser melted using different SLM processing parameters and the subsequent aging was carried out for the SLM Al−Mn−Mg−Sc−Zr alloys. Based on this, the effects of solute supersaturation and re-precipitation on the mechanical properties of the SLM Al−Mn−Mg−Sc−Zr alloys were revealed.

2 Experimental

2.1 Materials

Table 1 shows the chemical compositions of the SLM Al−Mn−Mg−Sc−Zr alloy powders. The morphology of the metal powders was observed on a Nova nanoSEM430 field emission scanning electron microscope (SEM), as shown in Fig. 1. It can be seen that most of the powders are spherical and only a few irregular ellipsoidal powders exist. Besides, a few smaller powders adhere to the larger powders. Figure 1(b) shows the particle size distribution, obtained from the Mastersizer 3000 laser particle size analyzer. The particle size ranges from 4 to 40 μm, with the median size of 22.4 μm and the mean size of 26.1 μm. The overall particle size distribution is narrow. Particles up to 14.1 μm in size account for 10%, and particles up to 35.7 μm account for 90% of the total.

Table 1 Chemical compositions of alloy powder (wt.%)

Mn	Mg	Fe	Sc	Zr
4.87	1.42	0.052	0.63	0.20
Si	Cr	Ti	Zn	Al
0.10	0.0050	0.0022	0.0044	Bal.

In this work, a SLM laser power of 330 W was chosen based on our previous work [11]. To investigate the effects of energy density on microstructure and mechanical properties of the SLM alloys, scanning speeds varied from 700 to 1500 mm/s. The scan strategy is illustrated in Fig. 1(c). The direction of scanning was clockwise rotated by 67° between consecutive layers. The main parameters in the SLM process were as follows: a layer thickness of 0.03 mm, a scanning spacing of 0.09 mm, a hatch distance of 0.09 mm, a stripe width of 5 mm, and a substrate preheating temperature of 35 °C. The above parameters determine energy density (E_v, J/mm^3) through the following formula [23−26]:

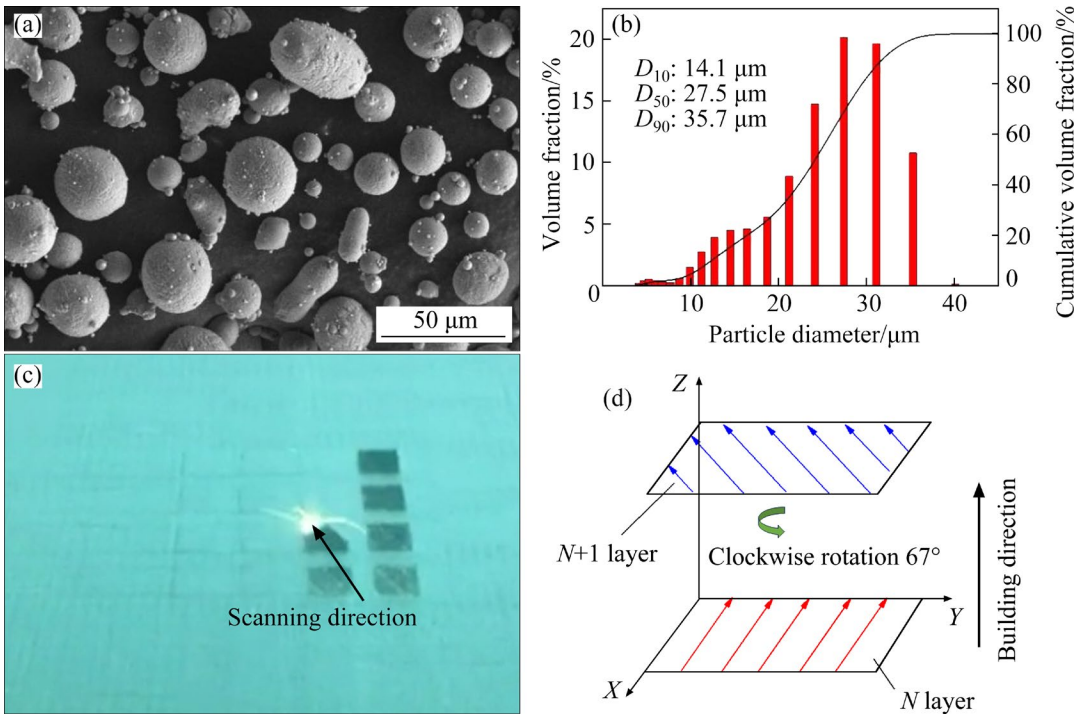

Fig. 1 SEM image (a), size distribution of SLM metal powders (b), scaning direction (c) and scanning strategy (d)

$$E_v=P/(vht) \quad (1)$$

where P is the laser power, h is the scanning spacing, t is the layer thickness, and v is the scanning speed. The corresponding E_v at each scanning speed is given in Table 2. The SLM Al−Mn−Mg−Sc−Zr alloys were aged at 300, 350, 400 and 450 °C for 8 h in the muffle furnace, respectively. Samples were air cooled after aging.

Table 2 Relationship between scanning speed and energy density

Scanning speed/(mm·s^{-1})	700	900	1100	1300	1500
Energy density/(J·mm^{-3})	175	136	111	94	81

2.2 Methods

Microhardness tests were carried out on the as-built and aged samples using an HVT−1000A Vickers hardness tester (loading force F=1.96 N, loading time t=15 s). The test was repeated three times. The tensile samples were fabricated directly by SLM, with the geometry reported in our previous work [11]. An MTS 810 tensile testing machine was used for tensile properties at room temperature with a tensile speed of 1 mm/min. The direction of the tensile test sample was perpendicular to the building direction.

The Nikon LV150N optical microscope (OM) with 220 V and 50 Hz power was used to observe and analyze the defects of the as-built aluminum alloys. The field 3D microscopy system (MTS−3000) was used to observe the surface roughness of SLM samples. The fracture morphologies of the SLM samples made at different scanning speeds were analyzed by SEM (Zeiss EVO10-3412). The surface elemental distributions of the as-SLM and aged specimens were characterized by a JXA−8230 electron probe microanalyzer. The grain size, morphology and phase distribution of the as-SLM and aged alloys were observed by a Titan G^2 60-300 transmission electron microscope. Phase identification and lattice distortion measurement were conducted using a Rigaku 2500 X-ray diffractometer (XRD) with a Cu K_α radiation (λ=0.154 nm), a scanning range of 20°−145° and a scanning speed of 1 (°)/min.

3 Results

3.1 SLM defects and surface roughness

Figure 2 shows OM images of the as-SLM alloys fabricated at different scanning speeds, observed from both the surface (vertical to the building direction) and the side face (parallel to the building

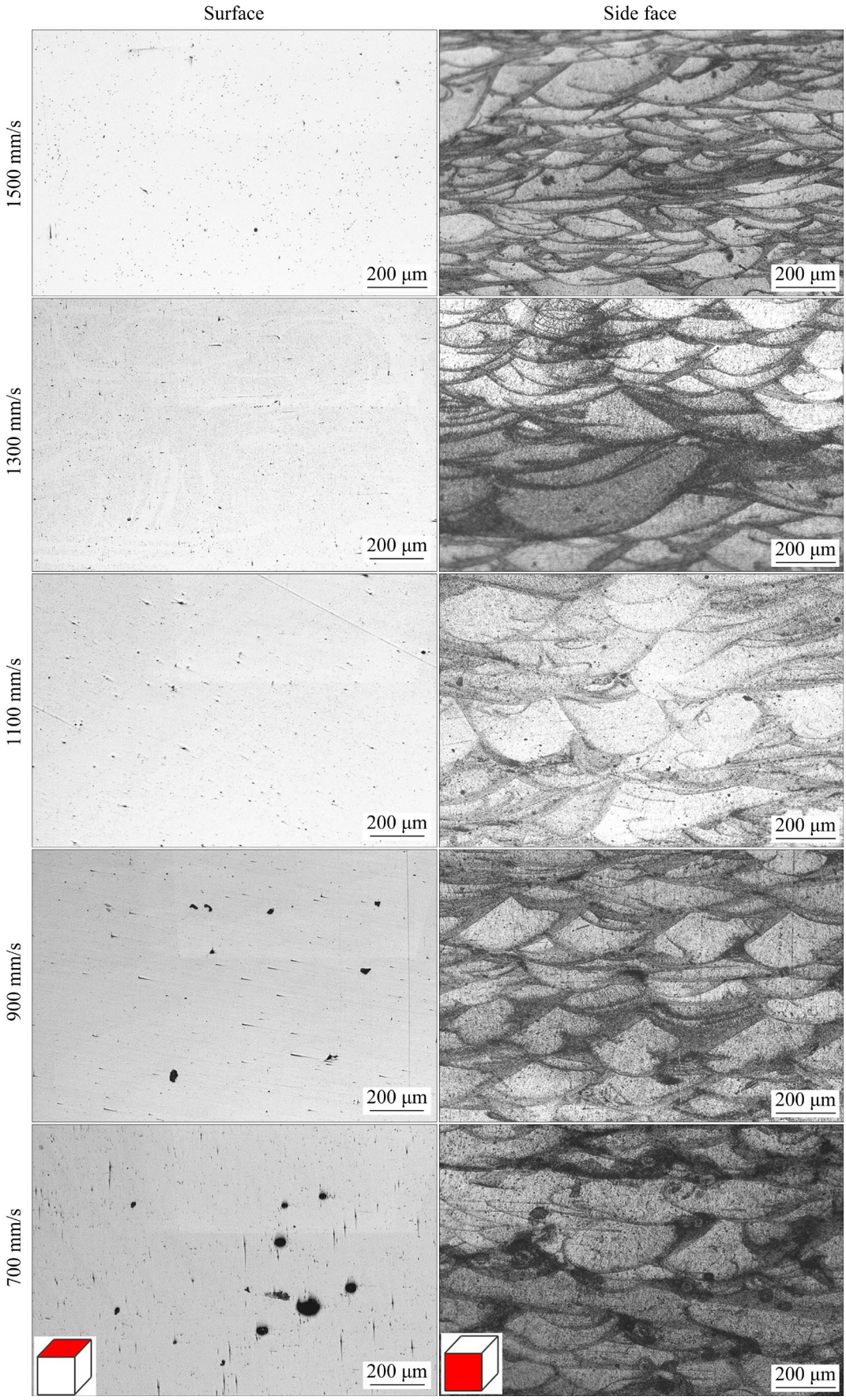

Fig. 2 OM images of SLM alloys fabricated at different scanning speeds

direction). Pores were detected on both the surface and side face of the as-SLM alloys. As the scanning speed increased, both the number and the size of cavities decreased, with the minimum SLM defects observed at the highest scanning speed of 1500 mm/s. When the scanning speed ranged from 1100 to 1500 mm/s, only a few pores existed on the SLM alloys. The reduced porosity at higher speeds is attributed to low energy density that allows the liquid metal to flow without splashing and to fill the pores which are formed in solidification shrinks.

Many fan-shaped areas can be observed in the OM images from the side face. These areas are the typical molten pool structure formed under SLM. During continuous scanning of the laser beam, the top of the solidified molten pool was heated and melted again by the subsequent laser beam, causing some overlap between the neighboring molten pools. As the scanning speed increased, the overlapping increased; at higher scanning speeds, the solidification time was reduced. The formation of fine grains at the molten pool boundary is mainly attributed to the precipitation of primary $Al_3(Sc,Zr)$ particles.

Figure 3 shows the surface roughness of the as-SLM alloys fabricated at different scanning speeds. The results show that increasing the scanning speed increased the surface roughness. Especially, when the scanning speed was greater than 1100 mm/s, some sharp protrusions could be seen. It can also be seen that the surface roughness of SLM samples shows a rising trend with the increase of scanning speed. This is because, at a higher scanning speed, less energy was absorbed, and less materials were melted. Therefore, after SLM, a larger number of partially melted powder particles appeared on the sample surface at a higher scanning speed, resulting in an increase in roughness.

3.2 Effects of scanning speed and aging treatment on hardness and mechanical properties

Figure 4 shows the hardness of the SLM alloys before and after aging at 300, 350, 400 and 450 °C for 8 h. It can be seen that the hardness slightly increased with the increase in the scanning speed. At high scanning speeds, such as 1300 and 1500 mm/s, the hardness values reach HV 125 and HV 126 in the as-SLM condition, respectively. Aging can significantly improve the hardness. For instance, for the SLM sample fabricated at the scanning speed of 1500 mm/s, aging at 350 °C for 8 h increased the hardness by about 30% to HV 174. However, further increasing aging temperatures above 400 °C decreased the hardness.

Figure 5 displays the stress−strain curves of the SLM Al−Mn−Mg−Sc−Zr alloys before and after aging at 350 °C for 8 h. The values of yield strength (YS), ultimate tensile strength (UTS) and elongation (EL) are listed in Table 3. The results show that the YS, UTS and EL of the SLM Al−Mn−Mg−Sc−Zr alloy increased with the increase in scanning speeds. Increasing scanning speeds from 700 to 1500 mm/s, the YS increased from 327 to 356 MPa, the UTS increased from 390 to 412 MPa, and the EL increased from 11.6% to

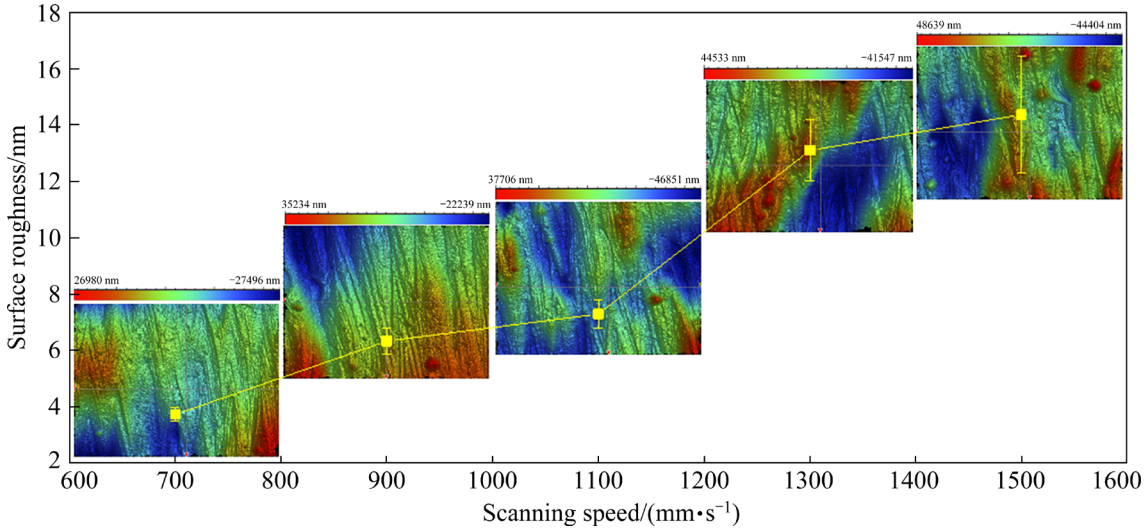

Fig. 3 Surface roughness of SLM alloys fabricated at different scanning speeds

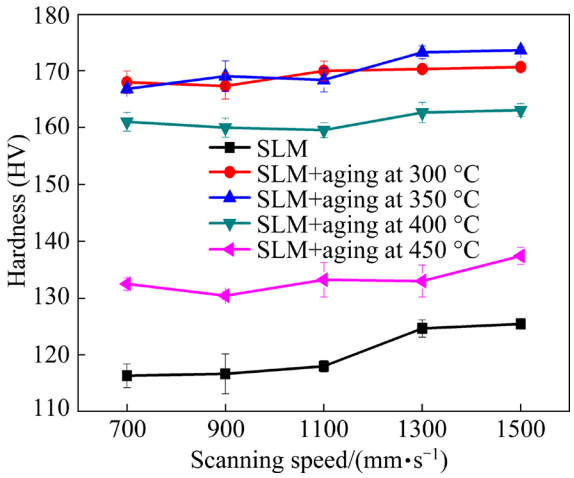

Fig. 4 Hardness curves of SLM alloys before and after being aged at different temperatures for 8 h

17.7%, respectively. The low EL of SLM Al−Mn−Mg−Sc−Zr alloys fabricated at low scanning speeds could be related to the existence of a large number of defects, such as cavities.

After aging at 350 °C for 8 h, YS and UTS of SLM Al−Mn−Mg−Sc−Zr alloys increased by more than 45% and 30%, respectively, for all the SLM samples fabricated at different scanning speeds. Meanwhile, strengthening through aging is more evident in samples fabricated at the higher scanning speeds. However, the elongation of SLM samples decreased after aging. The optimal mechanical properties were achieved in the aged SLM alloy at a scanning speed of 1500 mm/s, giving a YS of 527 MPa, a UTS of 554 MPa and an EL of 10.4%.

Figure 6 shows the tensile fracture morphologies of the SLM alloys fabricated at scanning speeds of 700, 1300 and 1500 mm/s, before and after aging. When the scanning speed was 700 mm/s, there existed a large number of large cavities on the fracture surface, with the pore sizes between 53 and 125 μm. This is because the metal powder absorbed too high energy per unit time when scanning speed was low, leading to the spheroidization phenomenon [27]. The mechanism of plastic fracture is the formation of micropores in the metal due to plastic deformation. As the stress increases, the micropores grow and combine with other micropores, resulting in the fracture of the alloys. Therefore, the SLM alloys fabricated at 700 mm/s with more cavities and defects formed

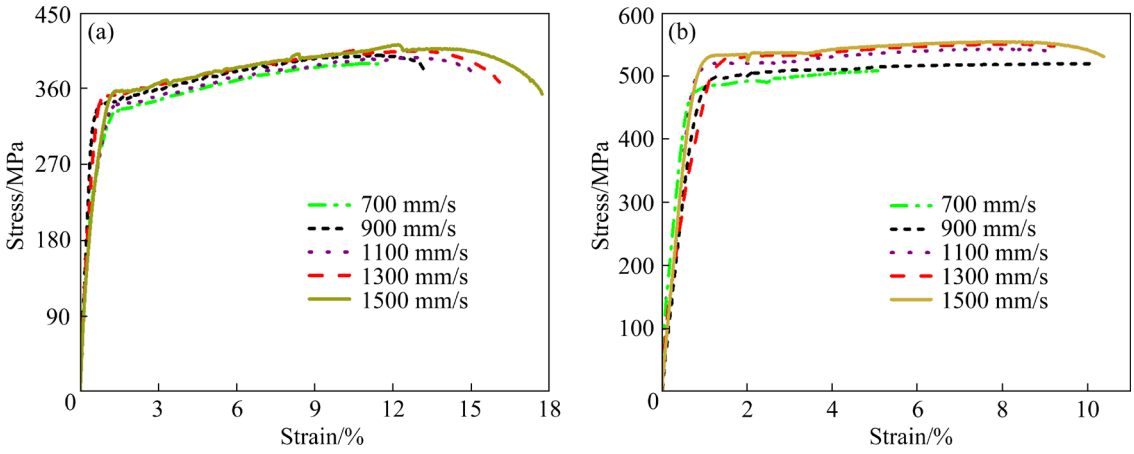

Fig. 5 Stress−strain curves of SLM alloys before and after aging treatment at different scanning speeds: (a) SLM; (b) SLM+aging

Table 3 UTS, YS and EL of SLM alloys before and after aging treatment

Scanning speed/(mm·s^{-1})	UTS/MPa		Increment of UTS/%	YS/MPa		Increment of YS/%	EL/%	
	SLM	Aged		SLM	Aged		SLM	Aged
700	390	508	30.3	327	482	47.4	11.6	5.2
900	400	520	30.0	335	491	46.6	13.4	10.0
1100	397	543	36.8	337	513	52.2	15.1	9.0
1300	407	550	35.1	346	528	52.6	16.0	9.2
1500	412	554	34.5	356	527	48.0	17.7	10.4

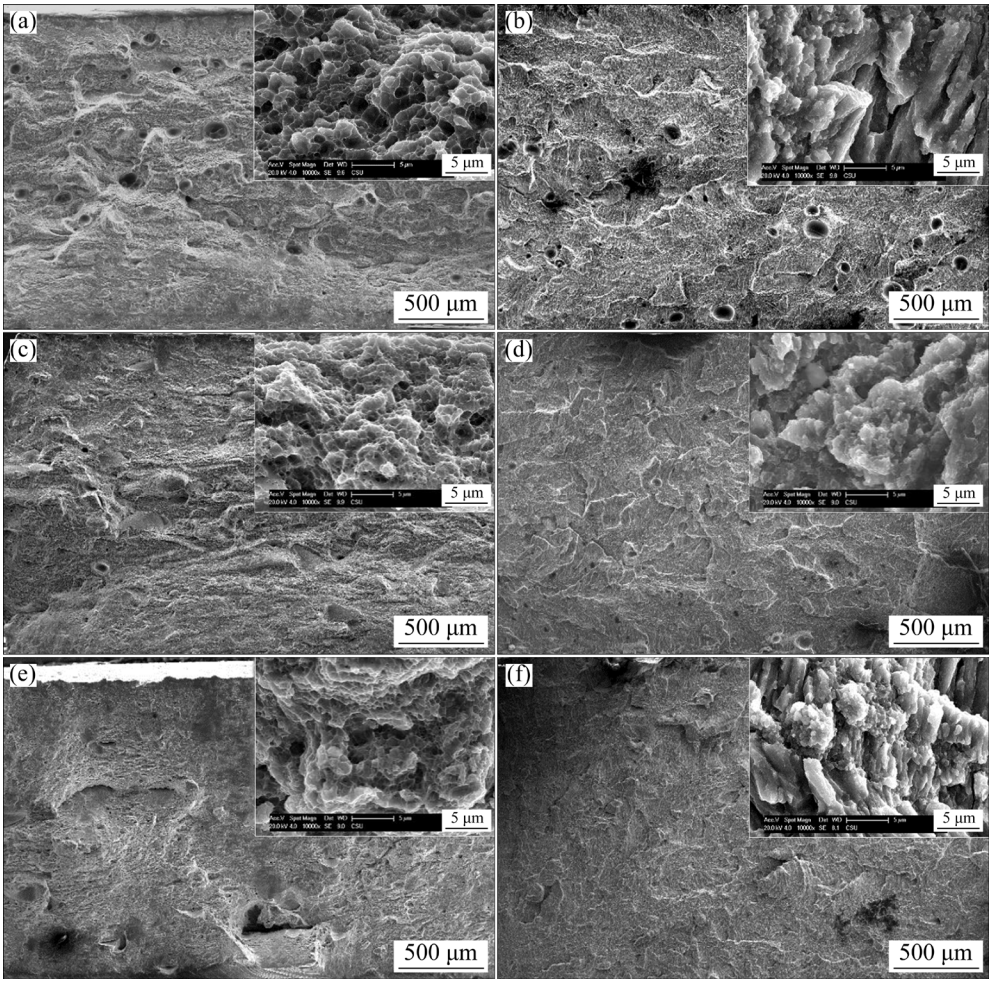

Fig. 6 Tensile fracture morphologies of SLM alloys fabricated at different scanning speeds before (a, c, e) and after aging treatment at 350 °C for 8 h (b, d, f): (a, b) 700 mm/s; (c, d) 1300 mm/s; (e, f) 1500 mm/s

during SLM processing were more prone to fracture and exhibited poorer plasticity.

After aging, dimples size decreased for all samples. This is because in SLM condition, the equiaxed crystals at the bottom of the molten pool were so small that samples started to fracture from the columnar crystal region in the center of the molten pool. However, after aging at 350 °C for 8 h, the equiaxed grains at the bottom of the molten pool grew and thus smaller dimples were formed. In all, the fracture mechanisms of the studied SLM alloys before and after aging are all ductile transgranular fracture mode.

3.3 Effect of scanning speed on solute atom super-saturation

The XRD patterns of the as-SLM alloys fabricated at scanning speeds of 700, 1300 and 1500 mm/s are shown in Fig. 7. Six obvious diffraction

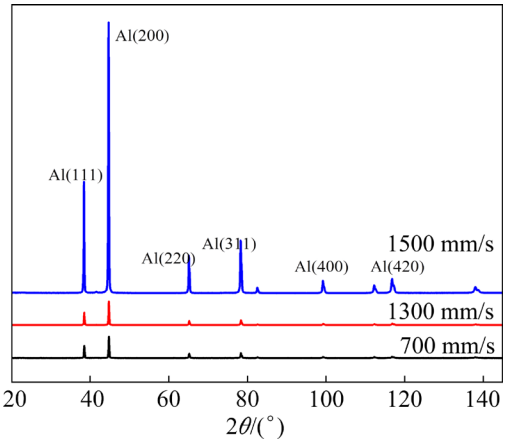

Fig. 7 XRD patterns of as-SLM alloys fabricated at different scanning speeds

peaks of Al matrix appeared, while the diffraction peaks of the possible precipitates rich in Mg and Mn were not detected. The maximum Al peaks at the three scanning speeds are all (200), showing a

preferred grain growth orientation towards the surface plane. With the increase in the scanning speed, the diffraction peak tends to shift to the left, and the diffraction peak at the high angle shows obvious broadening. This reveals that supersaturated solute atoms result in lattice distortion in the Al matrix. At scanning speeds of 1500, 1300 and 700 mm/s, the interplanar spacing values were calculated to be 0.20185, 0.20189 and 0.20218 nm, respectively; the corresponding lattice distortion values were 0.31%, 0.29% and 0.15%, respectively. The results showed that a higher degree of supersaturation was obtained in the Al matrix at high scanning speed.

3.4 Precipitation and re-precipitation

Figure 8 shows the electron probe images and elements mappings of the as-SLM and aged alloys fabricated at 700 and 1500 mm/s. The results show that micrometer-scale precipitates formed during SLM, but their number density reduced at higher scanning speed. According to the surface scanning results, Fig. 8(a), the intermetallic compounds are rich in Mn. After the heat treatment at 350 °C for 8 h, intermetallic compounds re-precipitated with smaller sizes compared to those in the as-SLM samples. Those intermetallic compounds are rich in Mn, Mg and Si. Moreover, the Mn content increases after aging.

Figure 9 shows scanning transmission electron microscopy-high-angle annular dark field (STEM-HAADF) images and super-EDS results of the SLM alloys fabricated at a scanning speed of 1500 mm/s before and after aging. In Figs. 9(a−c), the SLM alloys show typical cast eutectic structures, exhibiting significant dendritic segregation. There are two kinds

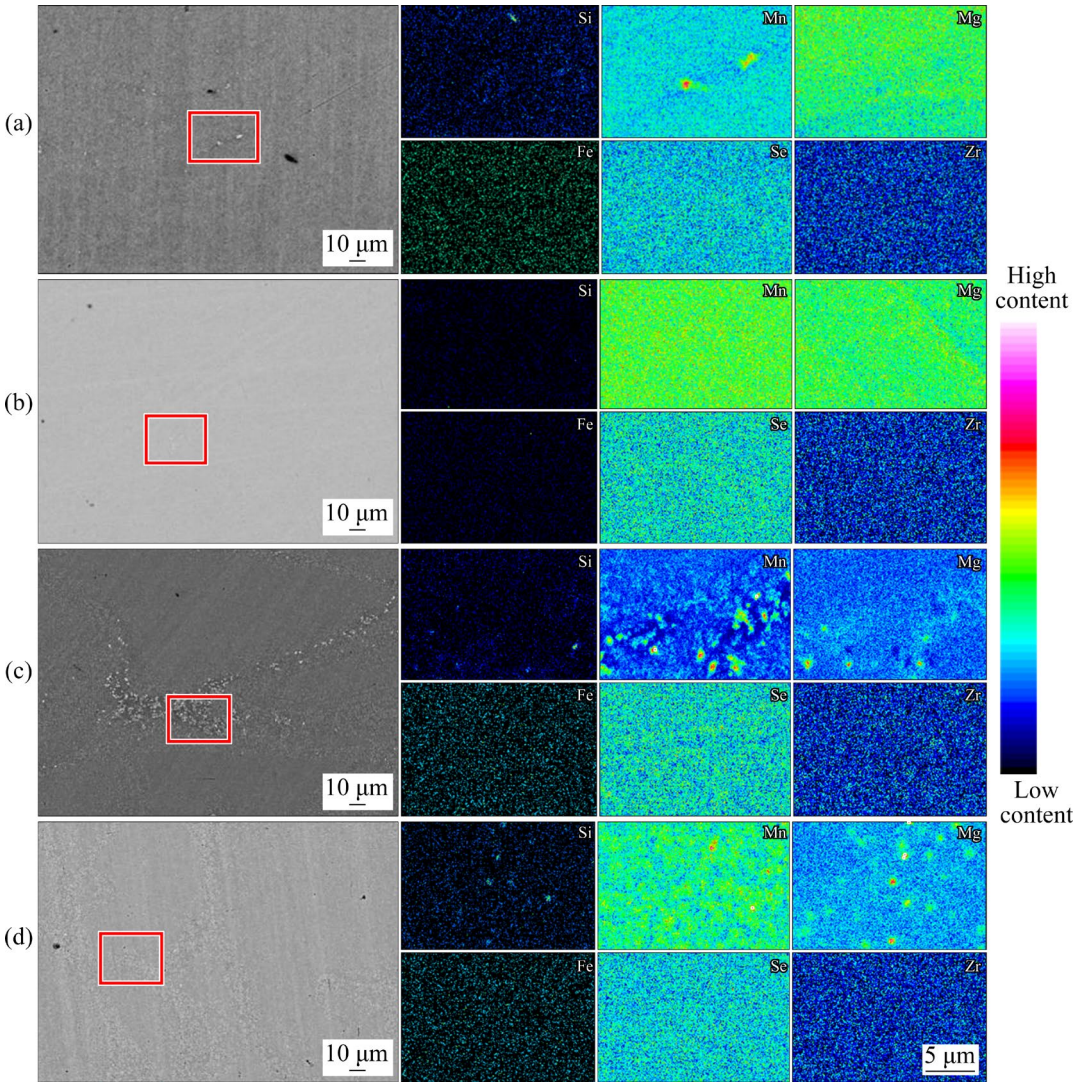

Fig. 8 Electron probe images and elements mappings of as-SLM and aged alloys fabricated at different scanning speeds before (a, c) and after aging treatment at 350 °C for 8 h (b, d): (a, c) 700 mm/s; (b, d) 1500 mm/s

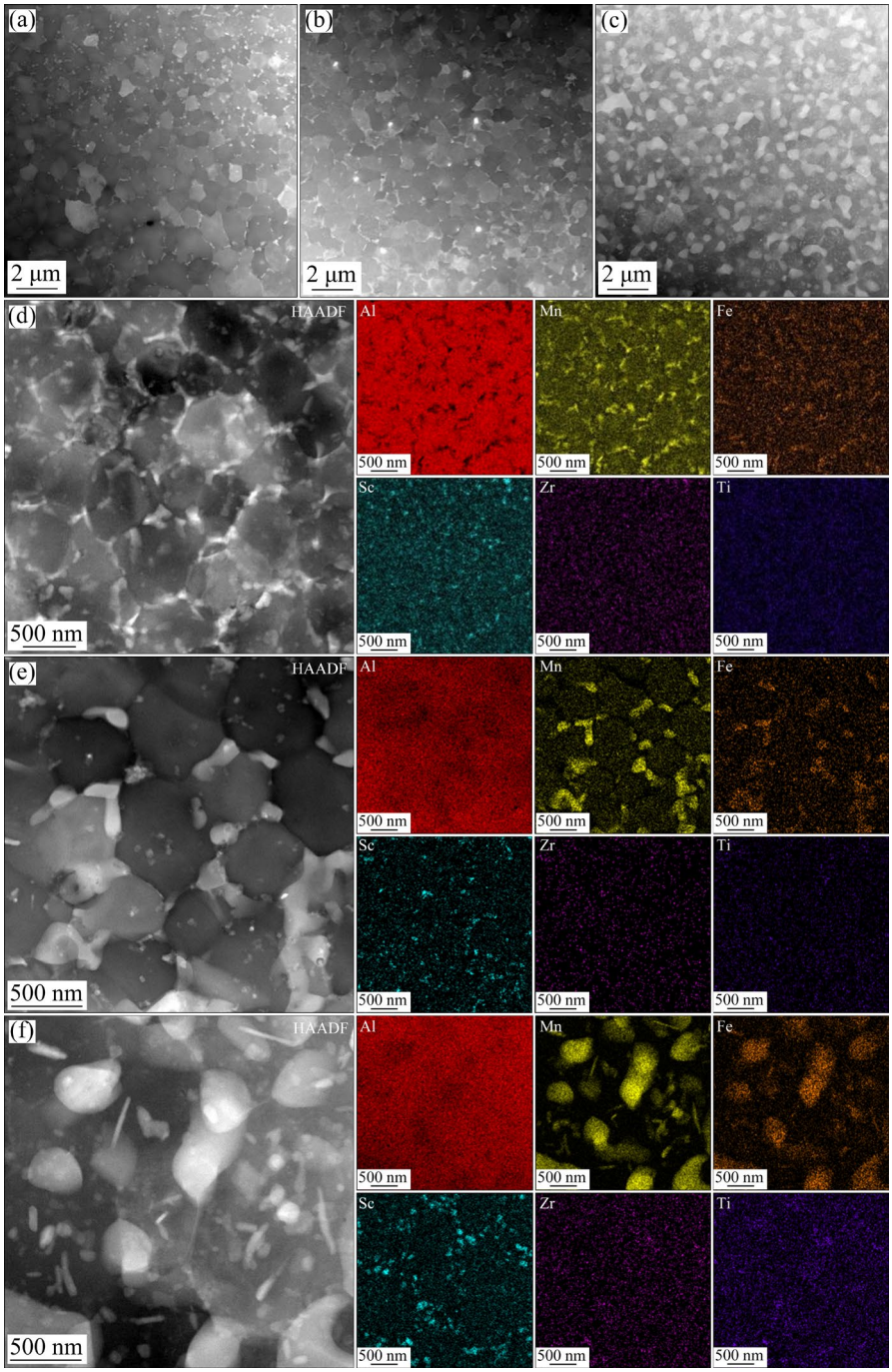

Fig. 9 STEM-HAADF images and super-EDS results of as-SLM and aged alloys fabricated at 1500 mm/s: (a, d) As-SLM; (b, e) Aged at 350 °C for 8 h; (c, f) Aged at 450 °C for 8 h

of intermetallic phases in SLM microstructure in Fig. 9(d). One is enriched in Mn and Fe at the grain boundary, and the other is enriched in Sc in the interior of grains. According to Refs. [24,25] about the SLM alloys with similar chemical compositions, the coarse phases at grain boundaries are identified as primary $Al_6(Fe,Mn)$ phase, and intragranular precipitates are identified as primary $Al_3(Sc,Zr)$ particles. Besides, the grains are equiaxed.

After aging at 350 °C for 8 h, the grain sizes increased and the grain boundary $Al_6(Fe,Mn)$ phases coarsened (Fig. 9(e)). Raising the aging temperature to 450 °C caused the grain boundary $Al_6(Fe,Mn)$ phases to grow (Fig. 9(f)), and the secondary $Al_6(Fe,Mn)$ needle-like phases formed within the grains. This indicates that the supersaturated Fe and Mn solute atoms in SLM alloys re-precipitated during high-temperature

aging. In additions Sc, Zr and Ti solute atoms also re-precipitated from the matrix. Due to the small size, the Sc, Zr and Ti enriched secondary phases were characterized by TEM bright-filed images and their crystal structures were confirmed by selective electron diffraction patterns (SADP) shown in Fig. 10.

Figure 10 shows TEM bright-field images and selective electron diffraction pattern (SADP) of the SLM alloys before and after aging at 350 °C for 8 h. For the as-SLM alloy, only a small number of Al_6(Fe,Mn) primary phases can be observed (Fig. 10(a)) , and only α(Al) matrix diffraction spots exist in SADP (Fig. 10(b)). After aging, secondary Al_6(Fe,Mn) needle-like appeared in the grains (Fig. 10(c)). Due to their small size, they were not detected in Fig. 9(e) of a lower magnification. Increasing the aging temperature to 450 °C, secondary Al_6(Fe,Mn) phases significantly grew, and they can be readily observed in Fig. 9(f). Besides, a large number of dispersive spherical particles can be seen in TEM bright-field images, as marked by the yellow arrows in Fig. 10(d). SADP in Fig. 10(e) shows that in addition to the matrix pattern, there are (010) and (110) superlattice spots. Combined with HAADF-EDS results in Fig. 9 and diffraction pattern in Fig. 10(e), it can be concluded that the nano-particles in Fig. 10(d) are the $L1_2$ structured Al_3(Sc,Zr,Ti), which precipitated during aging treatment.

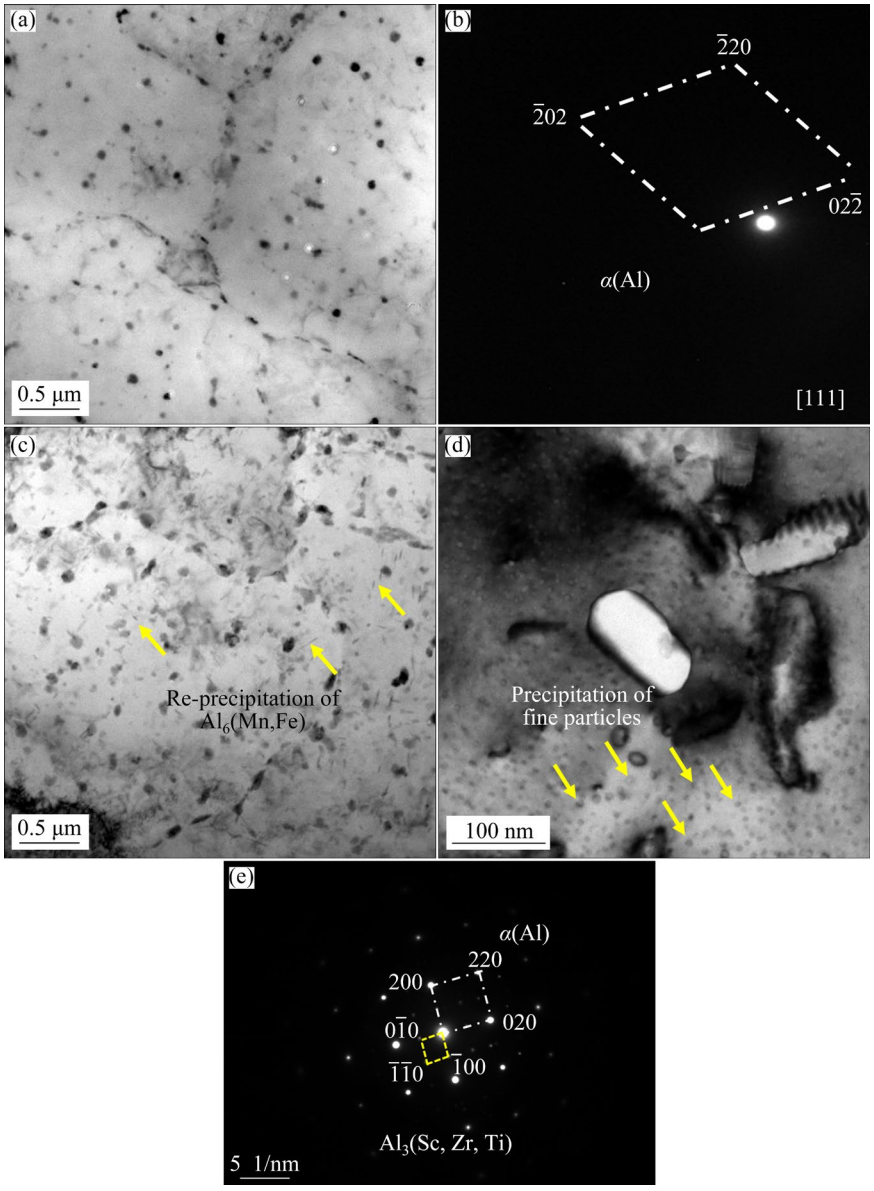

Fig. 10 TEM bright-field images (a, c, d) and selective electron diffraction patterns (SADP) (b, e) of as-SLM and aged alloys fabricated at 1500 mm/s: (a, b) As-SLM; (c−e) Aged at 350°C for 8 h

4 Discussion

4.1 Effects of solute atom supersaturation on strength

The results in this study showed that the Al−Mn−Mg−Sc−Zr alloy prepared at different SLM scanning speeds exhibited a large difference in mechanical properties. As the scanning speed increased, defects such as porosity in the alloy progressively decreased in size and number density, while the hardness, yield strength and tensile strength of the SLM samples gradually increased. When the scanning speed increased from 700 to 1300 mm/s, the hardness showed an obvious increase, but further increasing the speed to 1500 mm/s did not change the hardness much. Meantime, as the scanning speed increased from 700 to 1500 mm/s, the number density of the coarse intermetallic decreased significantly. Furthermore, their size became finer, and the distribution became more uniform. This is because the energy absorbed by the metal powder in the forming process is sufficient to melt it completely. Moreover, with the increase of the scanning speed, the temperature of the molten pool decreased, avoiding the occurrence of spheroidization phenomenon. In addition, by increasing scanning speeds, the degree of solute atomic supersaturation increased and the mean grain size decreased. For the SML samples of high scanning speed, solution strengthening and fine grain strengthening contributed to the strength, and fewer defects resulted in higher ductility, hence, better mechanical properties were obtained.

4.2 Effects of re-precipitation on strength

Because the SLM process has a fast-cooling rate of 103−108 K/s [26,27], it can help to obtain fine grain structure and high performance. During heat treatment of the SLM Al−Mn−Mg alloy, it is desired to minimize the grain growth for the performance of the alloy. It is found that aging improved the hardness of alloys. Among them, aging at 350 °C for 8 h resulted in the highest hardness improvement. Taking the sample of a scanning speed of 1500 mm/s as an example, after being aged at 350 °C for 8 h, the hardness increased from HV 125 to HV 174, the yield strength increased from 356 to 527 MPa, and the ultimate tensile strength increased from 412 to 554 MPa, each showing a gain of more than 35%.

Microscopy study results revealed that the characteristics of the phases in the SLM alloy changed significantly after heat treatment at different temperatures, which is illustrated in Fig. 11. In the SLM condition, there exist large primary $Al_6(Fe,Mn)$ phases at the boundaries (Fig. 9(d)). In the SLM process, the top of the molten pool of the previous layer was remelted and heated by subsequent laser deposition, which led to an instantaneous temperature increase for those primary $Al_6(Fe,Mn)$ phases to form [28−30]. After aging, spherical $L1_2$ structured $Al_6(Sc,Zr,Ti)$ nano-particles and needle-like secondary $Al_6(Fe,Mn)$ phases re-precipitated. When aging temperature increased to 450 °C, the secondary $Al_6(Fe,Mn)$ phases significantly coarsened (Fig. 9(c)). This is the main reason that the alloy aged at 350 °C shows a higher strength than the alloy aged at 450 °C.

4.3 Precipitation strengthening mechanisms

In this work, Al−Mn−Mg−Sc−Zr alloy was fabricated by SLM process at a laser power of 330 W and scanning speeds from 700 to 1500 mm/s.

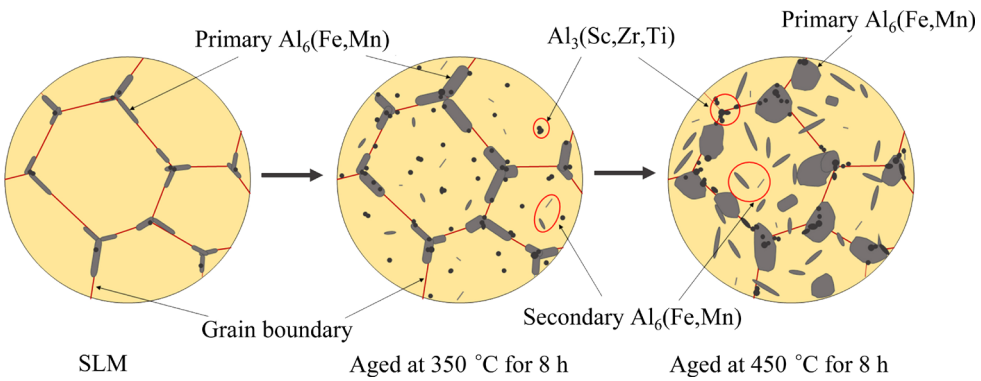

Fig. 11 Schematic diagrams of precipitation evolution

With the increase in scanning speeds, the solute atom supersaturation increased and the re-precipitation strengthening effect enhanced. At 1500 mm/s, after aging at 350 °C for 8 h, a high yield strength of 527 MPa was obtained. Figure 12 presents a survey of the tensile properties of SLM aluminum alloy reported in recent years [31−38]. The SLM samples in this study show excellent mechanical properties in both SLM and aging conditions.

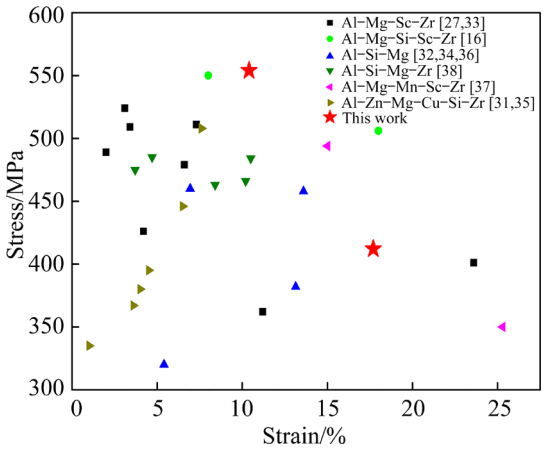

Fig. 12 Comparison of tensile mechanical properties of aluminum alloys in this work and Refs. [16,27,31−38]

After aging at 350 °C for 8 h, a high yield strength of 527 MPa was obtained. The main reason for the high strength of 3D printed Al alloy lies in the SLM process, where the top of the previous molten pool was reheated and melted by laser. This caused the materials on the top of molten pool to crystallize and form fine equiaxed grains. In addition, most Sc and Zr atoms dissolved in Al matrix during SLM, which were used to form the Al_6(Sc,Zr,Ti) nano- particles in high density during the heat treatment. Here, we analyzed the precipitation strengthening in Al alloys under SLM, 350 °C and 8 h aging and 450 °C and 8 h aging conditions, respectively.

There are two main mechanisms for achieving the high strength of the aged SLM alloys. For the as-SLM alloys, most of the Sc, Zr, Fe, Mn and Ti atoms were dissolved in the Al matrix during SLM manufacturing, leading to the higher solution strengthening. In addition, there were a large number of primary Al_6(Fe,Mn) phases. During aging, those supersaturated atoms re-precipitated to form spherical $L1_2$ structured Al_6(Sc,Zr,Ti) nano-particles and needle-like secondary Al_6(Fe,Mn) phases in high densities. Therefore, compared with the as-SLM alloys, the aged SLM alloys exhibited a lower supersaturation of solute atoms but a higher precipitation density. The precipitation strengthening effects were calculated by analyzing the microstructure of the as-SLM alloys before and after aging treatment at 350 °C for 8 h and 450 °C for 8 h, respectively.

There are two kinds of precipitation strengthening mechanisms in Al alloys. One is the shear strengthening mechanism for small particles, which include ordered strengthening, coherent strengthening and modulus strengthening. The other is the Orowan bypass mechanism for larger particles. As the size of precipitated particles increases to 4−6 nm, the strengthening mechanism changes from the former to the later [39−41]. The sizes of precipitated phases in this experiment are all above 6 nm, therefore Orowan mechanism is considered. The strength increase due to Orowan strengthening ($\Delta\sigma_{Or}$) is calculated as [42]

$$\Delta\sigma_{Or}=M\frac{0.4}{\pi}\frac{Gb}{\sqrt{1-\upsilon}}\frac{\ln\left(\frac{\pi d_m}{4b}\right)}{\lambda} \tag{2}$$

$$\lambda=\left(\frac{1}{2}\sqrt{\frac{2\pi}{3\varphi}}-1\right)\frac{\pi d_m}{4} \tag{3}$$

where M(=3.06) is the orientation factor of Al, b(=0.286 nm) is the amplitude of Burgers vector, φ is the volume fraction of the precipitated phase [43], G(=27.8 GPa) is the shear modulus of Al [41], λ is the effective particle spacing, d_m is the average particle radius, and υ(=0.331) is Poisson's ratio of Al [44]. The precipitates in as-SLM condition are primary Al_6(Fe,Mn) phases with an average diameter of 140 nm, thus the strength increment was calculated to be 62 MPa.

After aging at 350 °C for 8 h, as the primary Al_6(Fe,Mn) phase grew significantly, precipitation strengthening was negligible. The re-precipitated secondary fine Al_6(Fe,Mn) phases were needle-like and the precipitation strengthening was estimated by the following formula [24,45]:

$$\Delta\sigma_{Or}=0.13MG\frac{b}{2\sqrt{lr}}(\sqrt{f_v}+0.75\sqrt{\frac{l}{r}}f_v+0.14\frac{l}{r}f_v\sqrt{f_v})\ln\left(\frac{0.158l}{r_0}\right) \tag{4}$$

where l and r are the half-length and radius of needle-like precipitated phase, respectively, f_v is the volume fraction, and r_0 is the internal cut-off radius.

The re-precipitated secondary fine Al_6(Fe,Mn) phase and Al_6(Sc,Zr,Ti) nano-particles are the main strengthening phases in the aged alloys. The calculations showed that secondary Al_6(Fe,Mn) phase and Al_6(Sc,Zr,Ti) nano-particles contributed to an increment of 74 and 79 MPa in yield strength, respectively, and the combined precipitation strength increment was 153 MPa. The precipitation strengthening in 350 °C for 8 h aging condition is 91 MPa higher than that in the as-SLM condition. Increasing aging temperatures to 450 °C, the sizes of the secondary Al_6(Fe,Mn) phase increased significantly and its precipitation strengthening decreased to 24 MPa. For the Al_6(Sc,Zr,Ti) nano-particles, their size increased, but their density increased, which can be inferred from Figs. 9(e) and (f). The precipitation strengthening contribution of Al_6(Sc,Zr,Ti) was calculated to be 85 MPa. Table 4 lists the precipitation strengthening increments of precipitates in the as-SLM and aged alloys. It can be found that aging at 350 °C for 8 h can obtain higher precipitation strengthening increment. Increasing aging temperatures, the strength enhancement was normally dominated by the precipitation of nanosized secondary Al_6(Sc,Zr,Ti) precipitates.

Table 4 Precipitation strengthening increments

Precipitation phase	Precipitation strengthening increment/MPa		
	SLM	Aged at 350 °C for 8 h	Aged at 450 °C for 8 h
Al_6(Fe,Mn) phases	62	74	24
Al_3(Sc,Zr,Ti) re-precipitates	–	79	85
Total	62	153	109

5 Conclusions

(1) At the SLM laser power of 300 W, increasing scanning speeds from 700 to 1500 mm/s, the YS increased from 327 to 356 MPa, the UTS increased from 390 to 412 MPa, and the EL increased from 11.6% to 17.7%, respectively. Meantime, the lattice distortion values increased from 0.15% to 0.31%, indicating an increase in solute supersaturation.

(2) Aging treatment can significantly improve the mechanical properties of as-SLM alloys. Increasing the aging temperatures from 300 to 450 °C, the hardness increased firstly and then decreased. This was because during aging treatment, supersaturated solute atoms were re-precipitated in the form of secondary Al_6(Fe,Mn) needle-like phase and Al_6(Sc,Zr,Ti) nano-particles from the matrix, significantly strengthening the alloys. Further increasing aging temperatures, re-precipitated phases coarsened, and the strength decreased. 350 °C is a proper aging temperature.

(3) After aging at 350 °C for 8 h, the yield strength, the ultimate tensile strength and the elongation of as-SLM alloys reached 527, 554 MPa and 10.4%, respectively. The quantitative calculations show that the contributions of re-precipitated secondary Al_6(Fe,Mn) phase and Al_6(Sc,Zr,Ti) nano-particles to yield strength increment are 74 and 79 MPa, respectively. Increasing aging temperature to 450 °C, the precipitation strength enhancement was normally dominated by the nanosized secondary Al_6(Sc,Zr,Ti) nano-particles precipitates.

CRediT authorship contribution statement

Ying DENG: Supervision, Project administration, Writing − Review & editing; **Yi LAI:** Experiment, Writing − Original draft; **Jia-shun CHEN** and **Yuan-hao XU:** Methodology; **Jun-chang CAO:** Experiment; **Rui-yin HUANG:** Supervision; **Jia-qi DUAN:** Methodology, Writing – Review & editing.

Declaration of competing interest

The authors declare that they have no known competing financial interests or personal relationships that could have appeared to influence the work reported in this paper.

Acknowledgments

This work was financially supported by the Science and Technology Innovation Program of Hunan Province, China (No. 2023RC3055), the Natural Science Foundation of Hunan Province, China (Nos. 2023JJ30671), the Natural Science Foundation of Changsha City, China (No. Kq2208264), and the National Natural Science Foundation of China (No. 51601229).

References

[1] YOU Xiao-han, XING Zhi-quan, JIANG Shao-wei, ZHU Yao, LIN Yu-han, QIU Hua-sheng, NIE Ren-jie, YANG Jia-hao, HUI D, CHEN Wei, CHEN Yu. A review of research on aluminum alloy materials in structural engineering [J]. Developments in the Built Environment, 2024, 17: 100319.

[2] XU Guo-fu, LIU Liang, DENG Ying, ZENG Yu, CAO Jun-chang, TANG Lei, PENG Xiao-yan, DUAN Jia-qi, LIANG Mei-chan, PAN Qing-lin. Microstructure characteristics and corrosion behavior of metal inert gas welded dissimilar joints of 6005A modified by Sc and 5083 alloys [J/OL]. Transactions of Nonferrous Metals Society of China, [2024-09-13]. http://kns.cnki.net/kcms/detail/43.1239.TG. 20231118. 1237.002.html.

[3] LIU Liang, XU Guo-fu, DENG Ying, YU Qing-bin, LI Guo-liang, ZHANG Li-gang, Bing LIU, LE FU, PAN Qing-lin. Existing form of Sc in metal-inert gas welded Al−0.60Mg− 0.75Si alloy and its role in welding strength [J]. Materials Characterization, 2023, 197: 112649.

[4] YANG Yu-xi, GAO Wei-hong, SUN Bin, FU Yu-dong, MENG Xiang-long. Recent advances on additive manufactured shape memory alloys [J]. Transactions of Nonferrous Metals Society of China, 2024, 34(7): 2045−2073.

[5] GU D D, MEINERS W, WISSENBACH K, POPRAWE R. Laser additive manufacturing of metallic components: Materials, processes and mechanisms [J]. International Materials Reviews, 2012, 57: 133−164.

[6] LARROSA N O, WANG W, READ N, LORETTO M H, EVANS C, CARR J, TRADOWSKY U, ATTALLAH M M, WITHERS P J. Linking microstructure and processing defects to mechanical properties of selectively laser melted $AlSi_{10}Mg$ alloy [J]. Theoretical and Applied Fracture Mechanics, 2018, 98: 123−133.

[7] DENG Ying, CAO Jun-chang, LAI Yi, GUO Yi-fan, LIANG Mei-chan, PAN Qing-lin, XU Guo-fu. Effect of heat treatment on mechanical property and corrosion behavior of selective laser melted Al−Mn−Mg−Sc−Zr alloys [J]. The Chinese Journal of Nonferrous Metals, 2024, 34(4): 1240−1251. (in Chinese)

[8] GUO Yi-fan, LIAO Han-lin, CHANG Cheng, YAN Xing-chen, DENG Zhao-yang, DONG Dong-dong, CHU Qing-kun, DENG Ying, LIU Min. Effects of solute atoms re-dissolution on precipitation behavior and mechanical properties of selective laser melted Al−Mg−Sc−Zr alloys [J]. Materials Science and Engineering A, 2022, 854: 143870.

[9] YI Jiang-long, LIAO Han-lin, CHANG Cheng, YAN Xing-chen, LIU Min, ZHOU Ke-song. Reinforcing effects of nano-WC in $AlSi_{10}Mg$ alloy assisted by in-situ surface modification approach [J]. Transactions of Nonferrous Metals Society of China, 2024, 34(1): 50−64.

[10] MAO Yu, CHEN Hui, XIONG Jun. Research progress in laser additive manufacturing of aluminum alloys: Microstructure, defect, and properties [J]. Journal of Materials Research and Technology, 2024, 30: 695−716.

[11] LAI Yi, DENG Ying, ZHU Xin-wen, GUO Yi-fan, XU Guo-fu, HUANG Ji-wu, YIN Zhi-min. Tensile mechanical property and microstructure characteristics of a new Al−4.77Mn−1.37Mg−0.67Sc−0.25Zr alloy under different selective laser melting processing parameters [J]. Transactions of Nonferrous Metals Society of China, 2023, 33: 357−370.

[12] JIA Qing-bo, ROMETSCH P, CAO Sheng, ZHANG Kai, WU Xin-hua. Towards a high strength aluminium alloy development methodology for selective laser melting [J]. Materials & Design, 2019, 174: 107775.

[13] DU Lei, KE L, XIAO Mei-li, DOU En-hui, LUO Zhi-qiang, CHEN Yi, LAI Cai-fang. Densification, microstructure and properties of Sc and Zr modified Al−Mn alloy prepared by selective laser melting [J]. Optics & Laser Technology, 2022, 148: 107703.

[14] MAJEED A, ZHANG Ying-feng, LV Jing-xiang, PENG Tao, ATTA Z, AHMED A. Investigation of T4 and T6 heat treatment influences on relative density and porosity of $AlSi_{10}Mg$ alloy components manufactured by SLM [J]. Computers & Industrial Engineering, 2020, 139: 106194.

[15] SPIERINGS A B, DAWSON K, KERN K, PALM F, WEGENER K. SLM-processed Sc- and Zr-modified Al−Mg alloy: Mechanical properties and microstructural effects of heat treatment [J]. Materials Science and Engineering A, 2017, 701: 264−273.

[16] LI Rui-di, WANG Min-bo, LI Zhi-ming, CAO Peng, YUAN Tie-chui, ZHU Hong-bin. Developing a high-strength Al−Mg−Si−Sc−Zr alloy for selective laser melting: Crack-inhibiting and multiple strengthening mechanisms [J]. Acta Materialia, 2020, 193: 83−98.

[17] WANG Yan-fang, LIN Xin, KANG Nan, WANG Zi-hong, LIU Yu-xi, HUANG Wei-dong. Influence of post-heat treatment on the microstructure and mechanical properties of Al−Cu−Mg−Zr alloy manufactured by selective laser melting [J]. Journal of Materials Science & Technology, 2022, 111: 35−48.

[18] ZHANG Zhi-qian, LI De-hua, LI Sheng-ci, TANG Hui, ZHANG Yu, DONG Ting-ting, LI Wei-rong, LI Yan-fang, OLANREWAJU A O. Effect of post-heat treatment on the microstructure, mechanical, and corrosion properties of laser powder bed fused Al−Zn−Mg−Cu−Si−Zr−Er alloys [J]. Journal of Materials Research and Technology, 2023, 27: 1350−1364.

[19] MA Ru-long, PENG Chao-qun, CAI Zhi-yong, WANG Ri-chu, ZHOU Zhao-hui, LI Xiao-geng, CAO Xuan-yang. Effect of bimodal microstructure on the tensile properties of selective laser melt Al−Mg−Sc−Zr alloy [J]. Journal of Alloys and Compounds, 2020, 815: 152422.

[20] LIU Tong, WANG Qian-qian, CAI Xiao-ye, PAN Lu, LI Jian-sheng, ZONG Ze, CHENG Zong-hui, TIAN Zong-jun, LUO Liang-shun, SU Yan-qing. Effect of laser power on microstructures and properties of Al−4.82Mg−0.75Sc−0.49Mn−0.28Zr alloy fabricated by selective laser melting [J]. Journal of Materials Research and Technology, 2022, 18: 3612−3625.

[21] BI Jiang, LEI Zheng-long, CHEN Yan-bin, CHEN Xi, LU Nan-nan, TIAN Ze, QIN Xi-kun. An additively manufactured Al−14.1Mg−0.47Si−0.31Sc−0.17Zr alloy with high specific strength, good thermal stability and excellent corrosion

resistance [J]. Journal of Materials Science & Technology, 2021, 67: 23−35.

[22] BI Jiang, LIU Lei, WANG Chen-yang, CHEN Guang, JIA Xiang-dong, CHEN Xi, XIA Hong-bo, LI Xiao-peng, STAROSTENKOV M D, HAN Bing, DONG Guo-jiang. Microstructure, tensile properties and heat-resistant properties of selective laser melted AlMgScZr alloy under long-term aging treatment [J]. Materials Science and Engineering A, 2022, 833: 142527.

[23] CIURANA J, HERNANDEZ L, DELGADO J. Energy density analysis on single tracks formed by selective laser melting with CoCrMo powder material [J]. The International Journal of Advanced Manufacturing Technology, 2013, 68: 1103−1110.

[24] JIANG Wei, DENG Yun-lai, GUO Xiao-bin. Effect of heat treatment on microstructure and mechanical anisotropy of selective laser melted Al−Mn−Sc alloy [J]. Materials Science and Engineering A, 2023, 887: 145743.

[25] TANG Hao, GENG Yao-xiang, GAO Chao-feng, XI Xiao-ying, ZHANG Jian-tao, XIAO Zhi-yu. Microstructure evolution and mechanical properties of high-performance Al−Mn−Mg−Sc−Zr alloy fabricated by laser powder bed fusion [J]. Transactions of Nonferrous Metals Society of China, 2024, 34: 1413−1426.

[26] LI Yao, XU Guo-fu, PENG Xiao-yan, DENG Ying, YIN Zhi-min. Microstructure and mechanical properties of selective laser melting Al−Mg−Mn−Sc−Zr alloy annealed at different temperatures [J]. Transactions of Nonferrous Metals Society of China, 2022, 32: 1−19.

[27] WANG Zi-hong, LIN Xin, KANG Nan, HU Yun-long, CHEN Jing, HUANG Wei-dog. Strength−ductility synergy of selective laser melted Al−Mg−Sc−Zr alloy with a heterogeneous grain structure [J]. Additive Manufacturing, 2020, 34: 101260.

[28] BAYOUMY D, SCHLIEPHAKE D, DIETRICH S, WU X H, ZHU Y M, HUANG A J. Intensive processing optimization for achieving strong and ductile Al−Mn−Mg− Sc−Zr alloy produced by selective laser melting [J]. Materials & Design, 2021, 198: 109317.

[29] CHEN Jing, HOU Wei, WANG Xiu-zhuan, CHU Song-lin, YANG Zhi-yi. Microstructure, porosity and mechanical properties of selective laser melted $AlSi_{10}Mg$ [J]. Chinese Journal of Aeronautics, 2020, 33: 2043−2054.

[30] KEMPEN K, THIJS L, van HUMBEECK H J, KRUTH J P. Processing $AlSi_{10}Mg$ by selective laser melting: Parameter optimisation and material characterization [J]. Materials Science and Technology, 2014, 31: 917−923.

[31] ZHANG Zhi-qian, LI De-hua, LI Sheng-ci, DENG Hong-ling, ZHANG Si-yu, FANG Jin, YUAN Hao, DENG Bo, QI Liang. Effect of direct aging treatment on microstructure, mechanical and corrosion properties of a Si−Zr−Er modified Al−Zn−Mg−Cu alloy prepared by selective laser melting technology [J]. Materials Characterization, 2022, 194: 112459.

[32] BEN Dan-dan, MA Yun-rui, YANG Hua-jie, MENG Ling-xiao, SHAO Xiao-hong, LIU Hai-quan, WANG Shao-gang, DUAN Qi-qiang, ZHANG Zhe-feng. Heterogeneous microstructure and voids dependence of tensile deformation in a selective laser melted $AlSi_{10}Mg$ alloy [J]. Materials Science and Engineering A, 2020, 798: 140109.

[33] MA Ru-long, PENG Chao-qun, CAI Zhi-yong, WANG Ri-chu, ZHOU Zhao-hui, LI Xiao-geng, CAO Xuan-yang. Manipulating the microstructure and tensile properties of selective laser melted Al−Mg−Sc−Zr alloy through heat treatment [J]. Journal of Alloys and Compounds, 2020, 831: 154773.

[34] CAO Yang, LIN Xin, WANG Qing-zheng, SHI Shuo-qing, MA Liang, KANG Nan, HUANG Wei-dong. Microstructure evolution and mechanical properties at high temperature of selective laser melted $AlSi_{10}Mg$ [J]. Journal of Materials Science & Technology, 2021, 62: 162−172.

[35] LI Lan-bo, LI Rui-di, YUAN Tie-chui, CHEN Chao, ZHANG Zhi-jian, LI Xiao-feng. Microstructures and tensile properties of a selective laser melted Al−Zn−Mg−Cu (Al7075) alloy by Si and Zr microalloying [J]. Materials Science and Engineering A, 2020, 787: 139492.

[36] WU Hong, REN Yao-jia, REN Jun-ye, LIANG Lu-xin, LI Rui-di, FANG Qi-hong, CAI An-hui, SHAN Quan, TIAN Ying-tao, BAKER I. Selective laser melted $AlSi_{10}Mg$ alloy under melting mode transition: Microstructure evolution, nanomechanical behaviors and tensile properties [J]. Journal of Alloys and Compounds, 2021, 873: 159823.

[37] ZHAO Jun-hao, XUE Xiang, WANG Bin-bin, LIU Tong, LUO Lei, LUO Liang-shun, WANG Ya-nan, WANG Liang, SU Yan-qing, GUO Jing-jie, FU Heng-zhi. Selective laser melting Al−3.4Mg−0.5Mn−0.8Sc−0.4Zr alloys: From melting pool to the microstructure and mechanical properties [J]. Materials Science and Engineering A, 2021, 825: 141889.

[38] KNOOP D, LUTZ A, MAIS B, VONHEHL A. A tailored AlSiMg alloy for laser powder bed fusion [J]. Metals, 2020, 10: 514−527.

[39] FULLER C B, SEIDMAN D N, DUNAND D C. Mechanical properties of Al(Sc,Zr) alloys at ambient and elevated temperatures [J]. Acta Materialia, 2003, 51: 4803−4814.

[40] FAZELI F, POOLE W J, SINCLAIR C W. Modeling the effect of Al_3Sc precipitates on the yield stress and work hardening of an Al−Mg−Sc alloy [J]. Acta Materialia, 2008, 56: 1909−1918.

[41] KENDIG K L, MIRACLE D B. Strengthening mechanisms of an Al−Mg−Sc−Zr alloy [J]. Acta Materialia, 2002, 50: 7−13.

[42] WU L M, WANG W H, HSU Y F, TRONG S. Effects of homogenization treatment on recrystallization behavior and dispersoid distribution in an Al−Zn−Mg−Sc−Zr alloy [J]. Journal of Alloys and Compounds, 2007, 456: 163−169.

[43] VO N Q, DUNAND D C, SEIDMAN D N. Improving aging and creep resistance in a dilute Al−Sc alloy by microalloying with Si, Zr and Er [J]. Acta Materialia, 2014, 63: 73−85.

[44] KRUG M E, MAO Z G, SEIDMAN D N, DUNAND D C. Comparison between dislocation dynamics model predictions and experiments in precipitation-strengthened Al−Li−Sc alloys [J]. Acta Materialia, 2014, 79: 382−395.

[45] LIU Gang, ZHANG Gui-jun, DING Xiang-dong, SUN Jun, CHEN Kang-hua. Modeling the strengthening response to aging process of heat-treatable aluminum alloys containing plate/disc- or rod/needle-shaped precipitates [J]. Materials Science and Engineering A, 2003, 344: 113−124.

溶质原子过饱和度及再析出对选区激光熔化 Al−Mn−Mg−Sc−Zr 合金显微组织和力学性能的影响

邓 英[1]，赖 毅[1]，陈嘉顺[1]，许元浩[1]，曹俊昌[1]，黄瑞银[2]，段佳琦[3]

1. 中南大学 材料科学与工程学院，长沙 410083；
2. 中铝材料应用研究院有限公司，北京 102209；
3. Warwick Manufacturing Group, The University of Warwick, Coventry, CV4 7AL, UK

摘 要：通过选区激光熔化技术制备一种新型 Al−4.87Mn−1.42Mg−0.63Sc−0.25Zr(质量分数, %)合金，研究合金时效前后的显微组织和力学性能。结果表明：在 300 W 的激光功率下，随着激光扫描速度从 700 mm/s 增至 1500 mm/s，合金的力学性能提高，与此同时，点阵畸变从 0.15%增至 0.31%，溶质原子过饱和程度增加。在 1500 mm/s 的激光扫描速度下，选区激光熔化合金的屈服强度、极限抗拉强度和伸长率分别为 356 MPa、412 MPa 和 17.7 %。经 350 ℃时效 8 h 后，选区激光熔化合金的屈服强度、抗拉强度和伸长率分别达到 527 MPa、554 MPa 和 10.4%。时效中重新析出的二次针状相 Al_6(Fe,Mn)和具有 $L1_2$ 结构的 Al_6(Sc,Zr,Ti)纳米相分别贡献了 74 MPa 和 79 MPa 的屈服强度增量。当增加时效温度至 450 ℃时，析出强化以 Al_6(Sc,Zr,Ti)纳米粒子占优势。

关键词：Al−Mn−Mg 合金；选区激光熔化；再析出；溶质原子；显微组织；力学性能

(Edited by Wei-ping CHEN)